J Appl Physiol 95: 657–671, 2003.
First published March 14, 2003; 10.1152/japplphysiol.00770.2002.

Gravitational deposition in a rhythmically expanding and contracting alveolus

S. Haber,[1] D. Yitzhak,[1] and A. Tsuda[2]
[1]*Department of Mechanical Engineering, Technion, Haifa 32000, Israel; and*
[2]*Physiology Program, Harvard School of Public Health, Boston, Massachusetts 02115*

Submitted 23 August 2002; accepted in final form 11 March 2003

Haber, S., D. Yitzhak, and A. Tsuda. Gravitational deposition in a rhythmically expanding and contracting alveolus. *J Appl Physiol* 95: 657–671, 2003. First published March 14, 2003; 10.1152/japplphysiol.00770.2002.—In a previous simulation, our laboratory demonstrated that the flow induced by a rhythmically expanding and contracting alveolus is highly complex (Haber S, Butler JP, Brenner H, Emanuel I, and Tsuda A, *J Fluid Mech* 405: 243–268, 2000). Based on these earlier findings, we hypothesize that the trajectories and deposition of aerosols inside the alveoli differ substantially from those previously predicted. To test this hypothesis, trajectories of fine particles (0.5–2.5 μm in diameter) moving in the foregoing alveolar flow field and simultaneously subjected to the gravity field were simulated. The results show that alveolar wall motion is crucial in determining the enhancement of aerosol deposition inside the alveoli. In particular, 0.5- to 1-μm-diameter particles are sensitive to the detailed alveolar flow structure (e.g., recirculating flow), as they undergo gravity-induced convective mixing and deposition. Accordingly, deposition concentrations within each alveolus are nonuniform, with preferentially higher densities near the alveolar entrance ring, consistent with physiological observations. Deposition patterns along the acinar tree are also nonuniform, with higher deposition in the first half of the acinar generations. This is a result of the combined effects of enhanced alveolar deposition in the proximal region of the acinus due to alveoli expansion and contraction and reduction in the number of particles remaining in the gas phase down the acinar tree. We conclude that the cyclically expanding and contracting motion of alveoli plays an important role in determining gravitational deposition in the pulmonary acinus.

alveolus expansion; lungs; chaos

INHALED FINE PARTICLES (0.5–2.5 μm in diameter) are likely to penetrate deep into the gas exchange region of the lung (3). Because these particles are too large to undergo significant thermal diffusion and too light to be substantially affected by inertia, their fate may predominantly be determined by the balance between aerodynamic and gravitational forces (13).

Until lately, it has been widely accepted that gravitational settling and deposition of fine particles deep inside the lung can reasonably be predicted, assuming that a simple Poiseuille flow can represent the flow field inside the acinus, ignoring completely the complexity of the flow that exists inside the alveoli. A mathematical model describing particle motion under gravity in a horizontal, long, straight pipe was originally given by Fuch (7) and Pich (20). It was later modified by Wang (30) and Hyder (12), who addressed the cases of particle motion inside inclining and declining pipes and randomly oriented pipes, respectively.

More recently, modifications to the foregoing "classic" model of the acinus were suggested, arguing that the alveolated structure of acinar ducts is likely to play a significant role in the acinar fluid mechanics and, consequently, in the transport of fine particles (25, 26). A simplified alveolar duct model included a rigid axisymmetric duct surrounded by toroidal pockets that opened to a central thoroughfare. The flow field was numerically solved, and trajectories of micrometer-sized particles were studied (26). The main finding of this initial investigation was that gas streamlines in the central channel were somewhat curved due to the presence of side-walled alveoli, and this curvature of the streamlines, coupled with the orientation of the duct relative to gravity, may cause the particles to enter the alveolus and deposit there. These findings were later confirmed by others (5, 6) in similar alveolated duct computer models.

Subsequently, the effect of an additional kinematic parameter, the rhythmical motion of the alveolar walls, on the flow was investigated. Sophisticated models of acinar fluid mechanics, representing time-dependent low Reynolds number flows in cyclically expanding and contracting alveolated duct structure, were developed (4, 8, 11, 24, 27–29). Both the theoretical and experimental analyses have demonstrated that fluid path lines in the acinus are highly complex. The forgoing complex flow patterns result in chaotic trajectories if *1*) asynchrony exists between ductal and expansion flows (8, 28), or *2*) inertial effects are considered (11, 27). These findings are of utmost importance and are significantly different from past investigations of alveolated rigid thoroughfares that resulted in periodic fluid path lines, which repeated themselves with every breathing cycle (5, 6, 25, 26). These findings also imply that models that fail to incorporate alveolar expansion and contraction may lead to incorrect pre-

Address for reprint requests and other correspondence: S. Haber, Dept. of Mechanical Engineering, Technion, Haifa 32000, Israel (E-mail: mersh01@tx.technion.ac.il).

The costs of publication of this article were defrayed in part by the payment of page charges. The article must therefore be hereby marked "*advertisement*" in accordance with 18 U.S.C. Section 1734 solely to indicate this fact.

dictions for the deposition of fine aerosols in the pulmonary acinus.

Two mathematical models of acinar flow in a rhythmically expanding and contracting alveolated duct structure were developed: *1*) the acinar ductal flow model (11, 27), including an axisymmetric, multiple-alveolated expandable duct model with a closed end, and *2*) the single-alveolus model (8), consisting of a fully three-dimensional (3D) cyclically expanding and contracting hemispherical alveolus subjected to a shear flow passing over the alveolar mouth. The former model (11, 27) is most suitable to study the bulk kinematic interaction between the central channel flow and alveolar entering and exiting flows and the associated aerosol behavior (e.g., deposition efficiency). The latter model (8), we believe, captures essential features of the 3D time-dependent flow field inside alveoli and may be used to study the detailed motion of aerosol particles that penetrate the alveoli, their duration of stay inside the alveoli, and their deposition locations on the alveoli walls.

The objective of this study was to investigate the influence of the flow field induced by the rhythmical expansion and contraction of alveolar walls on the gravitational motion of fine aerosol particles, by using the 3D, single-alveolus model (8). The results suggest that *1*) the rhythmical expansion and contraction of the alveolar walls and the associated fluid flow patterns have a major role in determining the trajectories of particles settling under gravity. Fine particles in the size range of $0.5 \sim 1$ μm in diameter are particularly sensitive to the detailed patterns of recirculating alveolar flows, resulting in highly nonuniform deposition distributions on the alveolar walls. *2*) The relative magnitude of alveolar recirculation flow to ductal shear flow passing over the alveolar opening (discussed in detail below) plays a significant role in predicting particle behavior inside the alveolus. Because this ratio varies along the acinar tree, the process of gravitational deposition at the entrance of the acinus may differ from that at the periphery of the acinus. *3*) Even a small gravitational drift of aerosol particles from the cyclic gas streamlines can cause a substantial convective mixing. This gravity-induced convective mixing enhances deposition on the alveolar walls. The new model reported here demonstrates that the existence of alveolar recirculation is a key factor in determining the gravitational deposition in rhythmically expanding and contracting alveoli.

MATERIALS AND METHODS

In our laboratory's previous study (8), we investigated the time-dependent airflow inside lung alveoli by calculating the flow field $\mathbf{v}$ that is induced by cyclically expanding and contracting single-alveolar walls. In the present study, we analyze the behavior of spherical fine particles of diameter D_p ($0.5 \leq D_p \leq 2.5$ μm) and mass m_p of unit density (= 1 g/cm^3) suspended in the foregoing oscillating flow field. To make this paper self-contained, we recapitulate briefly the underlying assumptions of the flow model and the key characteristics of the flow field (8). This is followed by the detailed methods that are employed to track the motion of a suspended particle under the effect of gravitational forces.

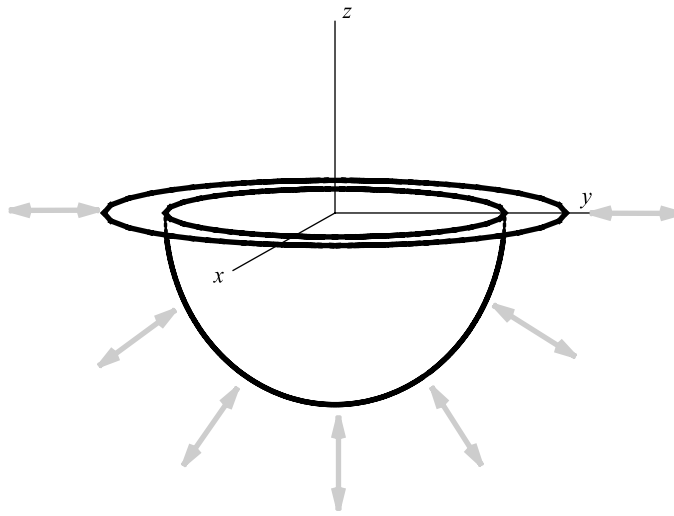

Fig. 1. Geometrical model of a single alveolus consisting of a rhythmically, self-similar expanding, hemispherical cavity attached to a rhythmically stretching plane. The shear flow far from the cavity is in the *y* direction.

Alveolar Flow Model

Our model views a single-alveolus configuration as a hemispherical cavity[1] attached at its rim to a flat plane (Fig. 1). The flow passing through the alveolar duct near the alveolus is approximated by a simple oscillatory shear flow over the flat plane, far upstream or downstream from the semispherical cavity. The plane and the attached cavity perform an oscillatory, self-similar expansion and contraction movement. Assuming that the flow field is governed by the creeping flow equations, superposition of the following two flow fields is allowed: *1*) the flow induced by the self-similar expansion and contraction of the alveolus with zero downstream flow inside the adjacent airway, and *2*) the flow induced by shear flow over a hemispherical rigid cavity with a vanishing velocity at the boundaries. Moreover, due to the quasi-steadiness of Stokes flows, the time variable can be viewed as a parameter that enters the problem via time-dependent boundary conditions. Thus two generic problems are addressed: the flow field $\mathbf{v}^H$ induced by a unit surface radial velocity for a unit radius hemisphere (8), and the flow field $\mathbf{v}^P$ induced by a unit shear flow over a unit hemispherical cavity (21). The solution representations for $\mathbf{v}^H$ and $\mathbf{v}^P$ are provided in APPENDIX A.

The flow $\mathbf{v}$ inside the alveolus, which combines the effects of expanding and contracting alveolus and the shear-induced flow generated by the airflow in the adjacent duct, is

$$\mathbf{v} = \dot{R}(t)\mathbf{v}^H + R(t)G(t)\mathbf{v}^P \qquad (1)$$

where $\mathbf{v}^H$ and $\mathbf{v}^P$ are multiplied by their respective time protocols for alveolus expansion and contraction, $\dot{R}(t)$, and for

[1]The present paper focuses on hemispherical cavities, because flow fields for general spherical caps are yet unsolved. Haber et al. (8) provided a general solution for various shapes of expanding spherical caps. Alas, Pozrikidis (21) obtained a numerical solution for shear flows over semispherical cavities only. Thus mathematical investigation of the effect of various alveolar openings must be postponed until the flow fields induced by shear flow over a nonhemispherical cavity are addressed.

the oscillating shear-flow in the adjacent airway, $R(t)G(t)$, where $G(t)$ is the instantaneous shear rate at the airway wall. It is often treated (albeit not exact) that $R(t) = R_0\,[1 + \beta\cos(\omega t)]$ and, consequently, $\dot{R}(t) = -R_0\,\beta\omega\sin(\omega t)$, where ω is the breathing frequency, R_0 is the mean radius of the alveolus, and $R_0\beta$ is the expansion amplitude. The time protocol $R(t)G(t) = -R_0G_0\sin(\omega t + \delta)$ is assumed to possess an identical ω and a small phase difference δ ($\cong 10°$) that was physiologically observed by Miki et al. (19) [see Tsuda et al. (28) for further discussion]. The value of G_0 depends on the breathing volumetric flow and the alveolus location down the acinar tree. The ratio γ between the amplitudes of shear and expansion flows is given by

$$\gamma = G_0/\beta\omega \tag{2}$$

Alternatively, for $\delta = 0$

$$\gamma \approx \frac{8Q_D}{Q_A}\left(\frac{R_0}{R_D}\right)^3 \tag{3}$$

where Q_D is the instantaneous volumetric ductal flow passing by the alveolus, Q_A is the instantaneous volumetric flow entering the alveolus, and R_D is the mean radius of the acinar duct adjacent to the alveolus. Using the acinar morphology data by Haefli-Bleuer and Weibel (9), γ was computed (see APPENDIX B) and plotted as a function of Weibel's airway generation number (Fig. 2). The value of γ at the first few generations (e.g., 16 ~ 19th) from the entrance of the acinus is >1,000 and remains >100 for most of the acinar generations, suggesting that the ductal shear flow plays an important role in determining alveolar flow. In previous studies (8, 11, 27), we found that a sufficiently strong shear flow passing by the alveolar opening induces vortexes inside the alveolus, and the presence of alveolar recirculation flow in an expanding and contracting alveolus indicates the existence of a stagnation saddle point in the alveolar flow field. Figure 5, *A* and *B*, from Haber et al. (8) depicts streamline maps of such cases ($\gamma = 400$ and 200, respectively, with $\delta = 0$). Within very few generations from the distal end of the acinar tree, the value of γ is of the order of 10. This suggests that the effects of alveolar wall motion are dominant and that alveolar flow is largely radial with no recirculating flows [see Fig. 5*D* from Haber et al. (8) for $\gamma = 20$ and $\delta = 0$].

Particle Motion

The differential equation governing the motion of a spherical particle subjected to the gravity field $\mathbf{g}$ is

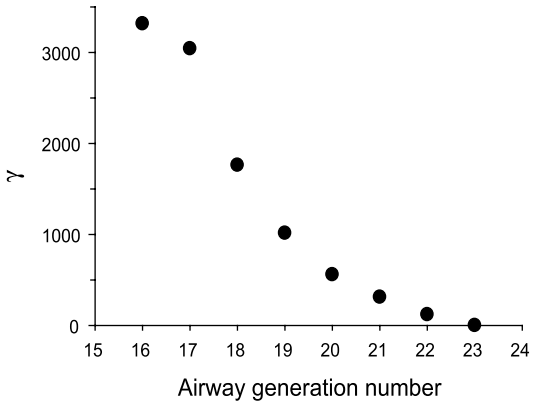

Fig. 2. The dependence of γ on the airway generation along the acinar tree (see APPENDIX B). The parameter γ also represents the ratio between the flow shear rate at the wall of the acinar duct to the strain rate of the alveolus.

$$m_p\frac{d\mathbf{v}_p}{dt} = \mathbf{F}_D + m_p g\hat{\mathbf{g}} + \mathbf{F}_{Br} \tag{4}$$

where $\mathbf{v}_p$ is the particle velocity, $\hat{\mathbf{g}}$ is a unit vector along $\mathbf{g}$, and $\mathbf{F}_D$ and $\mathbf{F}_{Br}$ are the respective drag and stochastic Brownian forces exerted on the particle. Henceforth, we focus on the combined deterministic effects of convection and sedimentation and neglect the stochastic Brownian forces (see the rationale of our approach in the DISCUSSION section).

The drag force exerted on a spherical particle suspended in a Stokesian flow field $\mathbf{v}$ is given as (10)

$$\mathbf{F}_D = 3\pi\mu D_p(\mathbf{v} - \mathbf{v}_p)_{CV}/C \tag{5}$$

where μ is the air viscosity, the suffix CV stands for evaluation of the airflow at the particle's center of volume, and C is the slip correction factor. The value of C for particles 0.5 and 1.0 μm in diameter is 1.324 and 1.164, respectively. Note that the quasi-steady solution (*Eq. 1*) for the velocity field $\mathbf{v}(x,y,z)$ was obtained for a unit hemisphere, whereas the alveolar radius in our case varies with time. Thus the instantaneous coordinates of the particle center (x_p, y_p, z_p) must be normalized with the instantaneous radius $R(t)$ and only then introduced into *Eq. 1* to yield the proper velocity field that the particle encounters. Namely, the approximate drag force exerted on the particle is given by

$$\mathbf{F}_D = \frac{3\pi\mu D_p}{C}\left\{\mathbf{v}\left[\frac{x_p}{R(t)}, \frac{y_p}{R(t)}, \frac{z_p}{R(t)}\right] - \mathbf{v}_p\right\} \tag{6}$$

Introducing *Eqs. 1* and *6* into *Eq. 4* and rewriting it in a dimensionless form yields

$$\frac{m_p\omega C}{3\pi\mu D_p}\frac{d^2\hat{\mathbf{r}}_p}{d\hat{t}^2} = \frac{m_p g C}{3\omega R_0\pi\mu D_p}\hat{\mathbf{g}} - \left\{\beta\,[\sin(\hat{t})\mathbf{v}^H(\hat{\mathbf{r}}_p/\hat{R}) + \gamma\sin(\hat{t} + \delta)\mathbf{v}^P(\hat{\mathbf{r}}_p/\hat{R})] + \frac{d\hat{\mathbf{r}}_p}{d\hat{t}}\right\} \tag{7}$$

where

$$\hat{t} = \omega t, \quad \hat{\mathbf{r}}_p = (x_p/R_0, y_p/R_0, z_p/R_0), \quad \hat{R} = 1 + \beta\cos\hat{t} \tag{8}$$

For particles 0.5–2.5 μm in diameter and densities ~1 g/cm^3, the maximum value of the Stokes number (S_t) that determines the magnitude of the *lefthand* side term in *Eq. 7* is

$$S_t = \frac{m_p\omega C}{3\pi\mu D_p} \approx 4\cdot 10^{-4}$$

whereas the gravity number (H) is of the order of

$$H = \frac{m_p g C}{3\pi\omega\mu R_0 D_p} \approx 0.5 - 20$$

Consequently, *Eq. 7* governing the particle position in space can further be simplified by neglecting the inertia term, yielding a highly nonlinear, first-order differential equation in $\hat{\mathbf{r}}_p$

$$\frac{d\hat{\mathbf{r}}_p}{d\hat{t}} = H\hat{\mathbf{g}} - \beta\,[\sin(\hat{t})\mathbf{v}^H(\hat{\mathbf{r}}_p/\hat{R}) + \gamma\sin(\hat{t} + \delta)\mathbf{v}^P(\hat{\mathbf{r}}_p/\hat{R})] \tag{9}$$

The solution of *Eq. 9* depends on 10 independent dimensionless parameters. Three parameters define the particle's initial position $(\hat{x}_{p0}, \hat{y}_{p0}, \hat{z}_{p0})$. An additional three parameters pertain to the kinematics of the problem, namely, the relative amplitude between the shear velocity and the expansion velocity γ, the phase lag between the flows δ, and the dimensionless amplitude of alveolus expansion β. A single param-

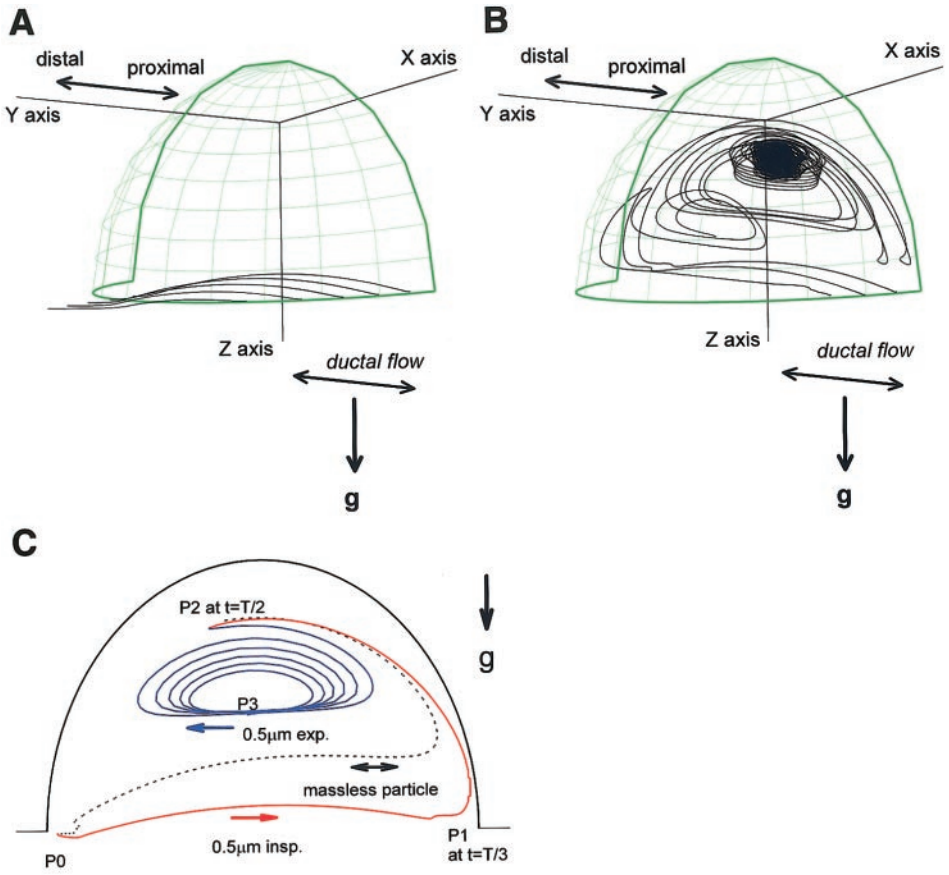

Fig. 3. Comparison between trajectories of 0.5-μm particles introduced into a rigid-walled alveolus (*A*) and a rhythmically expanding alveolus (*B*). In *A*, the particles do not enter the alveolus, whereas in *B*, the particles remain moving inside the alveolus, despite the pulling downward of the gravity force (g). *C*: comparison between the trajectories of a massless particle (a fluid particle, shown by a dotted curve) and a finite-sized particle moving in a gravitational field (the red and blue curves indicate motion during inspiration and expiration, respectively). The fluid particle returns to its initial position after a whole breathing cycle and exhibits a periodic motion. The massy particle performs a quasi-periodic motion. Flow parameters are $\gamma = 400$, $\beta = 0.1$, $x = 0$. P0–P2, *positions 0–2*; *t*, time; *T*, breathing period.

eter,[2] *H*, accounts for particle dynamics and is determined by the magnitude of the gravity field, the breathing frequency, the alveolus size, the fluid viscosity, and the particle size and density. Two parameters are required to define the direction of the gravity field $\hat{\mathbf{g}}$ with respect to the axes of symmetry of the alveolus and that of the adjacent duct (the *z* and *y* directions, respectively). The last parameter $\alpha = D_p/R_0$ that describes the ratio between sizes of the particle and the alveolus is required in determining gravitational deposition. Namely, integration of *Eq. 9* is terminated when the distance between the particle center and the alveolus wall is equal to its radius.

An analytic solution of the highly nonlinear set of three scalar first-order differential equations (*Eq. 9*) is a formidable task. A numerical approach is required that hinges on the data provided by Pozrikidis (21) and Haber et al. (8) for the vector fields $\mathbf{v}^P$ and $\mathbf{v}^H$, respectively. A detailed numerical procedure is given in APPENDIX C.

RESULTS

The behavior of a fine aerosol particle inside the acinus is determined by the balance between gravity and aerodynamic forces that are exerted on the particle. The magnitude of the gravitational force is proportional to the particle mass (neglecting buoyancy forces), and its direction is parallel to the unit gravity vector $\hat{\mathbf{g}}$. The magnitude and direction of the aerodynamic force, on the other hand, depend heavily on the local flow patterns and physical characteristics (size, shape) of the particles. As described in METHODS, there are a total of 10 independent dimensionless parameters affecting the motion of spherical particles. In this report, the investigation is focused on the three important parameters α, β, and γ that represent particle size, alveolus expansion amplitude, and alveolar location along the acinar tree, respectively. The effect of the gravity orientation on particle deposition awaits future investigation. Also, the lag angle δ is mostly kept zero in this report.

Effects of Alveolar Expansion

The effect of alveolar expansion on the behavior of aerosol particles may be best illustrated by tracking the motion of a particle in an alveolus whose opening is facing downward (Fig. 3). In the absence of wall motion (i.e., a rigid-walled alveolus; Fig. 3*A*), there is no upward air stream entering the alveolus, and particles cannot be convected into the alveolus. Furthermore, because the gravity force points downward, particles moving downstream shall simply bypass the alveolus. On the other hand, in case the alveolus performs a rhythmical expansion and contraction motion (Fig. 3*B*), an upward convection flow exists during inhalation. Thus particles can enter the alveolus, provided the aerodynamic drag force exerted on a particle mov-

[2] It is interesting to note that many physical properties are lumped into a single dimensionless parameter *H*. Thus, for instance, the effect of lowering particle density can be achieved by an equivalent increase of breathing rate.

ing upward can counterbalance the downward gravity force.

To demonstrate this delicate balance of forces in detail, the trajectory of a 0.5-μm particle initially placed near the alveolus rim is plotted in Fig. 3*C*. The trajectory of a massless (i.e., fluid) particle is also plotted for comparison. In both cases, the particles are passively introduced near the proximal corner of the alveolar opening [*position 0* (P0)] at the beginning of inspiration ($t = 0$). The fluid particle (shown as a dotted curve) enters the alveolus during inspiration ($0 < t < T/2$) and exits during expiration ($T/2 < t < T$), where T is the breathing period. Its trajectories during inspiration and expiration overlap; namely, the fluid particle undergoes a perfect kinematically reversible motion. The trajectory of an aerosol particle (shown as a solid curve) is, however, quite different. Starting at the same location (P0), it deviates from the path line of a fluid particle. During early inspiration ($0 < t < T/3$), the aerosol particle moves across the alveolar opening. At the time $t = T/3$ approximately, it approaches the distal corner of the alveolar opening (P1). The particle then continues moving upward into the alveolus against gravity and rotates along the expanding walls during the rest of the inspiration time ($T/3 < t < T/2$). The speed of aerosol movement is small during this period, because the tangential airflow velocities are typically small near the wall. At the end of inspiration ($t = T/2$), this aerosol particle is located deep inside the alveolus (P2). As the flow starts to reverse (i.e., early expiration), the velocity of airflow is nearly zero. During this time, therefore, gravity dominates the particle motion. Consequently, the particle starts to take an expiratory path, which is below the path taken during the late inspiration. This new path brings the particle to a region at the middle of the alveolus, where airflow is recirculating. Here, the particle rotates five and one-half times in the alveolus during the expiration period. At the end of the cycle ($t = T$), the particle remains suspended near the center of the alveolus (P3). In subsequent cycles (not shown), this particle continues to rotate in the alveolus, and, finally after a few cycles, the motion of the particle reaches steady state (rotating counterclockwise 8 times during inspiration and clockwise 8 times during expiration in this example). This particle never leaves and remains suspended inside the alveolus, a manifestation that a delicate balance between the gravitational force and the effects of alveolar recirculation flow has been achieved.

Particle Deposition in a Rigid vs. Cyclically Expanding and Contracting Alveolus

Although the present model is not designed for quantitative analysis (e.g., a determination of exact deposition concentration per alveolus), it can be used to compare the relative difference in wall deposition concentrations between a rigid-walled alveolus and a cyclically expanding and contracting alveolus. We simulate the behavior of an aerosol bolus (of width 40 μm, consisting of 0.5-μm particles) approaching an alveolus in the case of cyclically expanding and contracting vs. rigid-walled models. In both cases, the alveolus is placed horizontally with its mouth facing upward, and the ductal shear flow condition is kept constant at $\gamma = 400$ (the effects of γ are discussed below). The movement of the bolus is monitored during one breathing cycle, and the number of particles deposited inside the alveolus is counted (Table 1). Results show that, under equivalent ductal shear flow conditions, deposition in a cyclically expanding and contracting alveolus ($\beta = 0.05$ and 0.1) is substantially higher (an increase of 134 and 112%, respectively) than that observed in a stationary alveolus ($\beta = 0$). [Note that the parameter β (0.1, 0.05, and 0) indicates the extent of the alveolar volume expansion (30, 15, and 0%, respectively).] This clearly demonstrates the dominant role alveolar wall motion can play in enhancing particle deposition inside the alveoli.

Effects of Particle Size

For a constant mass density of 1 g/cm^3, the trajectories of $D_P = 0.5$, 1, and 2.5 μm are obtained (Fig. 4*A*). The alveolus is horizontally placed with its mouth facing upward, and the flow conditions are set at $\gamma = 400$. The particles are introduced at the beginning of inspiration ($t = 0$) in the duct near the proximal corner of the alveolar opening (P0). For a small particle (0.5 μm; see Fig. 4*A*, *top*), whose motion is strongly influenced by the local flow field, the flow patterns near P0 are critical in determining the fate of the particle. When the initial position P0 of a particle is slightly moved from the alveolar opening toward the strong ductal thoroughfare airstreams, the particle is likely to be convected downstream without entering the alveolus (trajectory shown as a green line). On the other hand, when the position P0 is close enough to the alveolar opening, the particle (shown in red) follows the airflow entering the alveolus (shown as a dashed line) and simultaneously settling due to gravity ($0 < t < 0.2T$). Inside the alveolus, the behavior of the particle depends on the extent of instantaneous alveolar recirculation flow. When the recirculation flow is strong (e.g., $0.1T < t < 0.4T$), the particle follows the recirculation path, but, when the strength of the airflow begins to diminish as the end of inspiration approaches (e.g., $0.4T < t < 0.5T$), the particle trajectory

Table 1. *Comparison between the total number of particles being deposited inside a rigid alveolus (normalized to unity) and that of an expanding and contracting alveolus*

Rigid-walled Alveolus, $\beta = 0.0$	Rhythmically Expanding Alveolus	
	$\beta = 0.05$	$\beta = 0.1$
1	2.34 (134%)	2.12 (112%)

β, Dimensionless amplitude of alveolus expansion. Ratio between amplitude of shear and expansion flows = 400. Particle diameter = 0.5 μm. Phase difference = 0°.

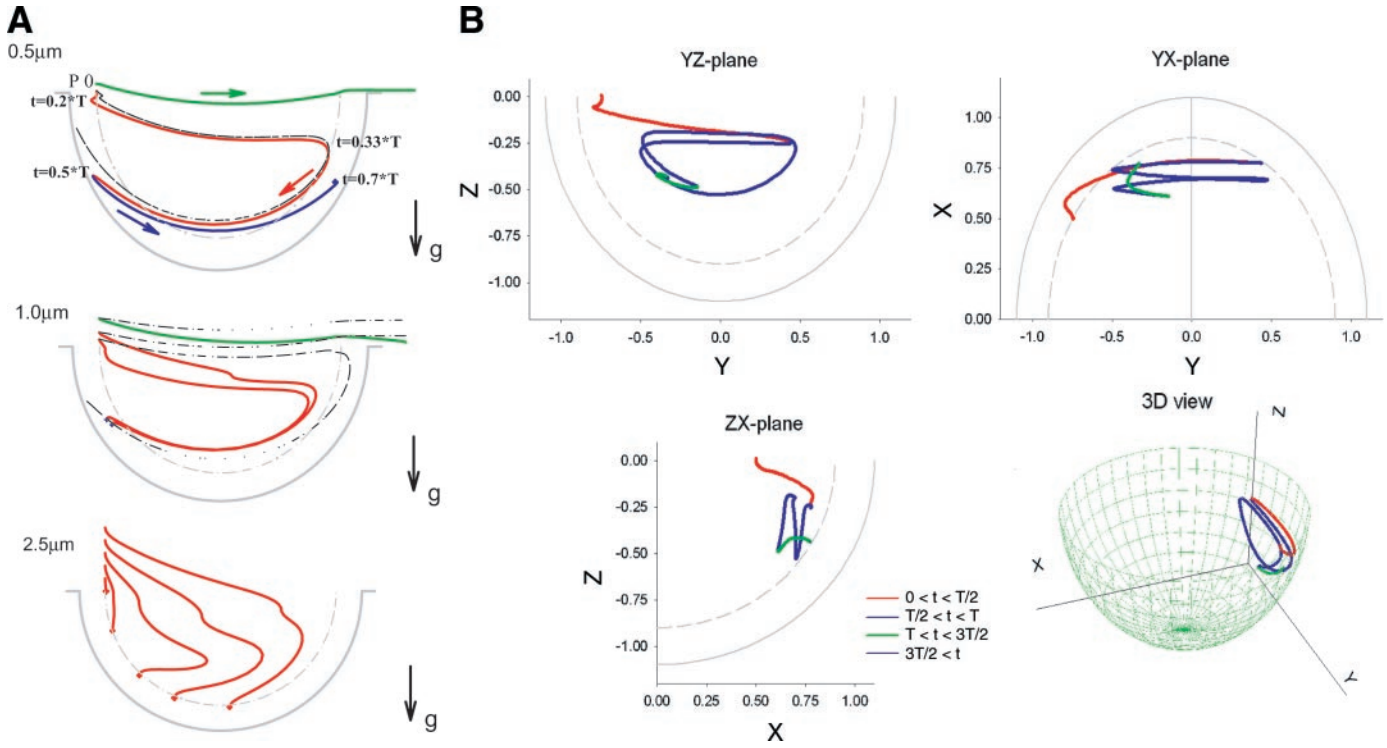

Fig. 4. *A*: trajectories of particles of different sizes. *Top*: light particles 0.5 μm in diameter closely follow path lines of fluid particles. *Middle*: medium-sized particles (1 μm) are moderately affected by gravity force. *Bottom*: heaviest particles (2.5 μm) are strongly affected by the gravity force. Flow parameters are $\gamma = 400$, $\beta = 0.1$, and $x = 0$. *B*: the trajectories of a particle initially placed off the symmetry plane at $x = 0.5$. A three-dimensional (3D) trajectory is depicted (*bottom right*), as well as three projections of the particle trajectory on the *zy*, *zx*, and *xy* planes.

starts to deviate from the fluid path line and drifts toward the alveolar wall due to gravity. During expiration, the particle moves back near the wall following the expiratory airflow (shown in blue) and continues to drift downward. Finally, the particle is deposited on the wall during the expiration period at $t = 0.7T$. The deposition process during expiration is augmented by the facts that airflow near the walls is generally weak and that the walls are contracting (i.e., moving toward the particle). It is interesting to point out that the direction of the particle's vertical drift due to gravity is opposite to that shown in Fig. 3*C* in which the particle moves away from the walls toward the alveolar center where the airflow is more intense.

The trajectory of a 0.5-μm particle initially placed off the midplane of the alveolus ($x \neq 0$) is very complex (Fig. 4*B*). During the inspiration period of the first cycle, the particle enters the alveolus and drifts appreciably toward the sidewall. This is due to the influence of substantial sideway airflow in the alveolus during inspiration (8). During expiration, it moves back toward the center of the alveolus while rotating one and one-half times. At the end of the first cycle, the particle remains suspended in the air deep in the alveolus. When the second inspiration starts, the particle moves again toward the sidewall, and, this time, this sideway motion soon causes the particle to be deposited.

For slightly larger particles (1 μm; see Fig. 4*A*, *middle*), the balance between the gravity and aerodynamic forces again plays an important role, determining whether the particles would enter the alveolus and be deposited. Despite the fact that 1-μm particles are eight times heavier than 0.5-μm particles (of equal density), their trajectories do not follow the gravity vector. If these particles enter the alveolus, they follow the alveolar recirculation paths and approach close to the walls, where the airflow velocity is nearly zero relative to the wall velocity, and finally deposition occurs (shown as short vertical turns of solid lines in Fig. 4*A*, *middle*). Most of the deposition sites are on the proximal side of the alveolar walls and occur during the end of inspiration (discussed below in detail).

For the largest particles (2.5 μm; see Fig. 4*A*, *bottom*), during the early stages of inspiration, the velocity of ductal airflow is still small, and the particles move appreciably downward due to gravity, entering the alveolus. Once the particles are inside the alveolus, they tend to follow the alveolar recirculation flow, especially during peak inspiration, but, due to their heavy weight, these 2.5-μm particles continue to settle downward and soon are deposited on the alveolar wall.

Deposition Site

The distribution of deposition sites inside the alveolus is determined for particles of different sizes (Fig. 5). About 1,000 particles of three different sizes (0.5, 1, and 2.5 μm) are equally spaced over the alveolar opening ($z = 0$) at $t = 0$. The simulation is performed at $\gamma = 400$ for a few cycles; for each cycle, the number of

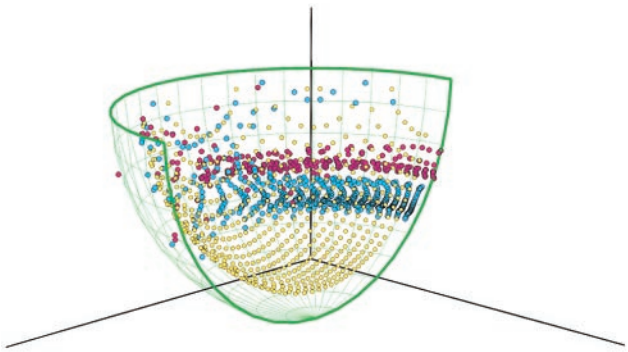

Fig. 5. Deposition location distributions for various particle sizes: 0.5 μm (pink), 1.0 μm (cyan), 2.5 μm (yellow). Particles are initially distributed at the alveolar opening. Flow parameters are $\gamma = 400$ and $\beta = 0.1$.

particles deposited on the alveolar walls and their deposition site are recorded. For 0.5-μm particles, ~47% of the particles enter the alveolus and deposit during the first cycle (41% during mid-to-late inspiration, 6% during early expiration). The deposition distribution of 0.5-μm particles on the alveolar walls is highly nonuniform, with a peak on the proximal side of the alveolar wall at about one-third of the way from the rim to the bottom (see pink symbols in Fig. 5; the deposition peak further moves closer to the rim as γ increases, as discussed later). All of the medium-sized particles (1.0 μm in diameter) deposit during the first cycle, mostly at the peak inspiration (92%), whereas few particles (8%) deposit at peak expiration. The deposition distribution of 1.0-μm particles is also nonuniform, with a peak on the proximal side of the alveolus at about midway from the rim to the bottom (see cyan symbols in Fig. 5). It is the area that the particles reach convectively after following the recirculation airflow during inspiration. As expected, the larger the particles are, the quicker the deposition occurs. For 2.5-μm particles, almost all of the particles (99%) deposit during the early inspiration period of the first cycle. These large particles are mainly deposited at the bottom region of the alveolus. The deposition distribution deep in the alveolus is nearly uniform, with a slight elevation on the proximal side (see yellow symbols in Fig. 5).

Gravitational Deposition Along the Acinar Tree (The Effects of γ)

As described in METHODS, the structure of alveolar flow is determined by the combined effects of the alveolar recirculation flow induced by ductal shear flow (Q_D) and alveolar entering and exiting radial flow (Q_A) induced by the rhythmic motion of the alveolar walls. Because the relative magnitude of Q_D to Q_A rapidly decreases as the tidal air moves deeper into the acinus, the velocity profile of the ductal flow entering the alveolus and the velocity field inside the alveolus are expected to change along the acinar tree, a change represented by the parameter γ. Consequently, we expect that the parameter γ has a significant influence on *1*) the efficiency of particles entering the alveolar cavity and *2*) the gravitational deposition process of particles inside the alveolus. We test this idea by simulating the motion of 0.5-μm particles near and inside the alveolus for various values of γ.

A sheet of equally spaced (~1,000) particles is placed over the alveolar opening at $t = 0$, and the number of particles entering the alveolus η, expressed as an "alveolar-entering efficiency," is examined for different values of γ (3,000, 800, 400, 200, 100, and 10) (Fig. 6*A*). For high values of γ (say, $\gamma = 3{,}000$, which corresponds to the alveolar flow near the entrance to the acinus, see Fig. 2), a relatively small number of particles enter the alveolar cavity, especially from the proximal side of the alveolar opening, and are deposited on the proximal side of the alveolar walls near the rim. As the value of γ decreases (corresponding to the alveolar flow deeper into the acinus, see Fig. 2), the η increases. At $\gamma \leq 100$, all of the particles released at the alveolar surface enter and are deposited. For comparison, a similar simulation is performed for the case of a rigid-walled alveolus, with the latter showing that the number of particles entering a rigid-walled alveolus is much smaller than that for an expanding alveolus for equivalent values of γ (see η_{rigid} in Fig. 6*A*).

Approximately 6,500 particles, equally spaced, are also placed inside the alveolus, and their behavior is monitored for different values of γ. For high values of γ (e.g., 3,000, 1,000), deposition occurs mainly during the early phase of inspiration (Fig. 7). The number density distribution of deposited particles is decidedly nonuniform, with a very high density on the proximal side close to the alveolar rim (Fig. 6*B*, *top*). For lower values of γ, but still higher than 100 (a range that corresponds to the majority of the acinar generations, except the very distal ones), the results are basically similar to those of $\gamma = 3{,}000$, namely, deposition occurs mainly during the first half of the inspiration period (Fig. 7) and preferentially on the proximal side of the alveolar wall surface (Fig. 6*B*, *middle*) further down from the rim. Remarkably, the deposition process is different in the case of $\gamma = 10$ (corresponding to the flow conditions occurring at the very distal alveoli). In this case, deposition is almost temporally invariant throughout two breathing cycles (Fig. 7), and deposition sites are spread almost uniformly on the alveolar surface (Fig. 6*B*, *bottom*), in sharp contrast to the cases of larger γ values (Figs. 6*B*, *top* and *middle*).

Convective Mixing Induced by Gravity

To further demonstrate the effects of alveolar flow patterns on gravitational deposition, the behavior of a cloud of aerosols compared with that of massless (i.e., fluid) particles is investigated. The flow parameters are kept constant, assuming the following values, $\beta = 0.1$, $\gamma = 400$, and $\delta = 0°$ (i.e., no phase lag exists between the expansion and the tidal shear flows). A small square-shaped cloud of massless particles (that exemplifies particle behavior in a gravitation-free environment) is introduced at the middle of the alveolus symmetry plane, $x = 0$ (Fig. 8*A*), and its behavior is

monitored through one breathing cycle. During inspiration, the initially square-shaped cloud is stretched and progressively deforms to an arc shape (pink symbols for $T/4$; gray symbols for $T/2$). During expiration, however, this large arc shrinks into a smaller arc (blue symbols for $3T/4$), with exactly the same shape as the one obtained at $t = T/4$, and finally it returns to the original square shape as the expiration process terminates (green symbols for $t = T$). As expected, the path of each massless particle is perfectly reversible under the simulated flow conditions ($\delta = 0°$ and Reynolds number = 0). In other words, during expiration, each particle faithfully retraces the path it outlined during inspiration, and, as a result, the square-shaped cloud is restored after a full cycle.

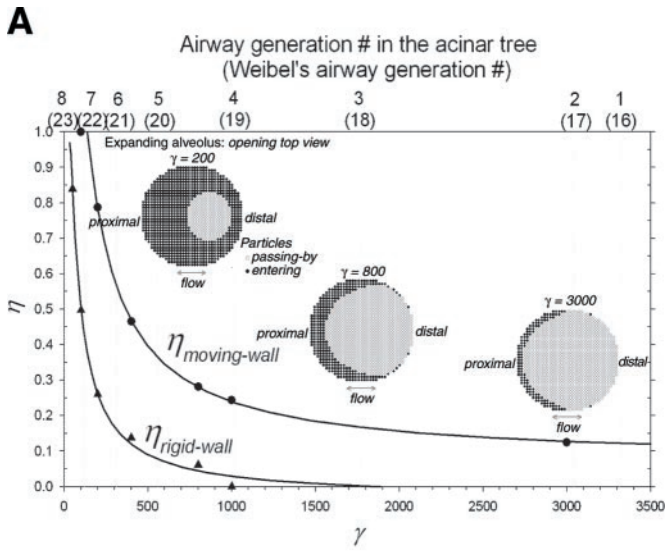

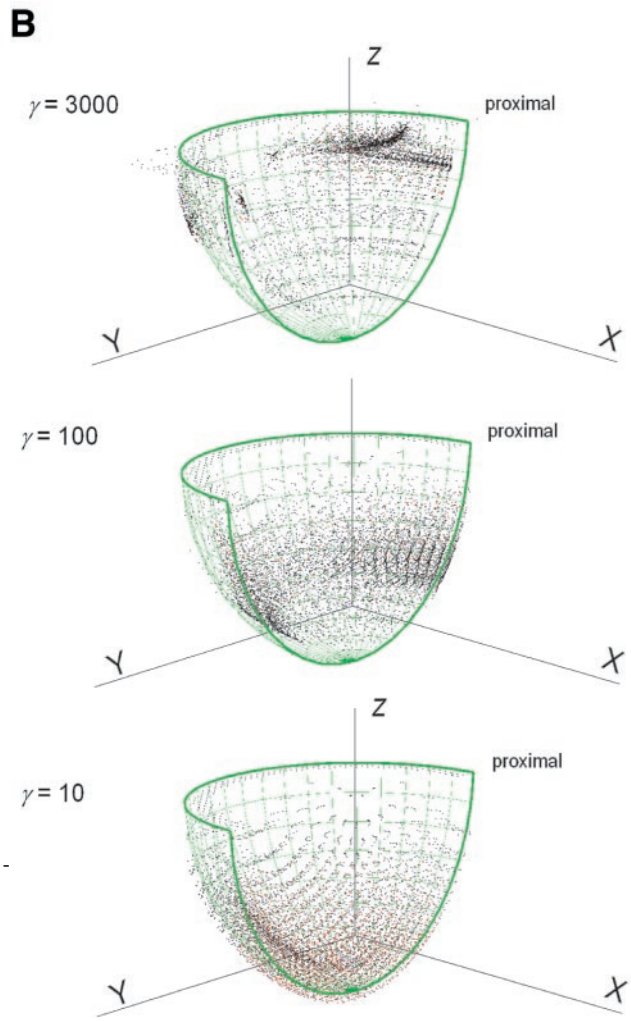

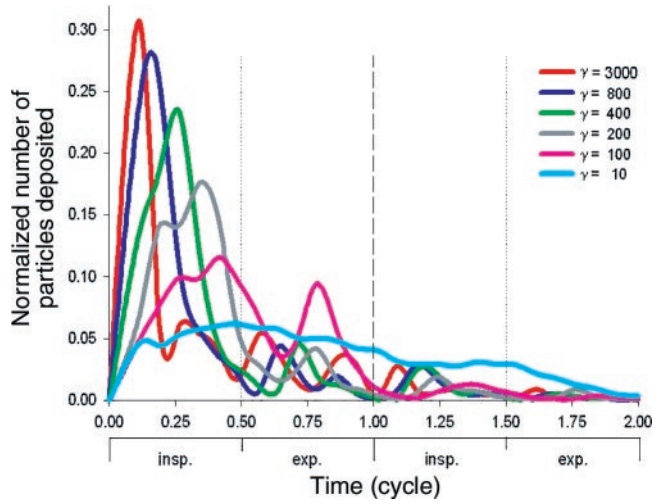

Fig. 7. No. of 0.5-μm particles deposited on the alveolar wall is normalized by the total no. of particles initially filled in the alveolus and plotted as a function of time. The figure demonstrates clearly that, for large values of γ (i.e., alveoli located high on the acinar tree), deposition rates are peaked during inspiration of the first breathing period. For medium values of γ, deposition occurs mainly during the first breathing period and is less peaked. For the small value of $\gamma = 10$ that corresponds to the very last acinar generation, deposition rate is almost constant throughout the breathing process.

In the simulation illustrated in Fig. 8*B*, a small square-shaped cloud of 0.5-μm particles (shown in black) is introduced at the middle of the alveolus at $t = 0$, and its behavior in a gravity field is monitored through a period of three cycles. Up until the end of the first inspiration period, the cloud of 0.5-μm particles behaves somewhat similar to that of the massless particles, namely, the square-shaped cloud possesses an elliptical shape at $t = T/2$ (shown in gray). However, by the end of the first cycle, the cloud of aerosol particles possesses a spiral shape (shown in green), instead of

Fig. 6. *A*: alveolar entering efficiency η as a function of γ for rhythmically expanding and contracting ($\eta_{moving\text{-}wall}$) and rigid-walled ($\eta_{rigid\text{-}wall}$) alveoli. *Insets* show the fate of 0.5-μm particles initially placed over the alveolus mouth. *B*: locations of 0.5-μm particle deposition for various γ values. Black, red, and blue dots represent deposition during the first, second, and third breathing cycle, respectively. *Top*: for a large value of γ (that corresponds to alveoli located high at the acinar tree), most particles are deposited near the rim with a pronounced peak near the proximal end of the alveolus. *Middle*: for a medium value of γ, particles concentrate at the mid-distance between the rim and the bottom of the alveolus, near the proximal end, with a more diffused distribution. *Bottom*: for a small value of γ, the particles concentrate close to the bottom of the alveolus, with no pronounced preference between the proximal and the distal ends.

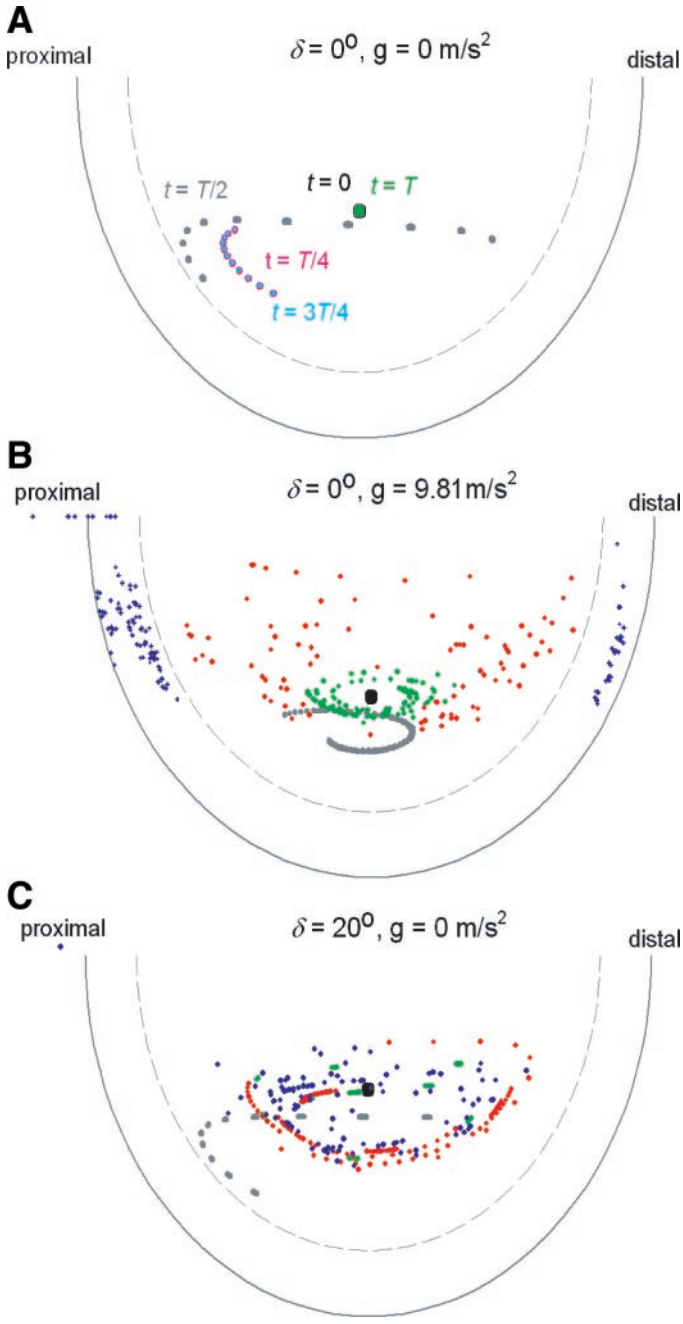

Fig. 8. A small bolus of particles (marked by a small square) is placed initially at the middle of the alveolus and tracked at different times during the breathing process. *A*: gravitation-free depiction of bolus locations at different times. Pink, gray, and blue dots pertain to $t = T/4$, $T/2$, and $3T/4$, respectively. For $t = T$, after a complete breathing period, the bolus returns to its initial position. *Middle*: same as *top* for location of a bolus affected by gravity during 3 breathing periods. Gray, green, and red dots pertain to $t = T/2$, T, and $2T$, respectively. Blue dots stand for particle deposition locations during the second breathing cycle. *Bottom*: same as *top*, only here the phase lag between shear and expansion-induced flows is nonzero. Gray, green, red, and blue dots pertain to $t = T/2$, T, $2T$, and $3T$, respectively.

returning to its original square shape, demonstrating that the trajectory of each particle is not kinematically reversible. Irreversible spreading continues during the second cycle, and the initial square shape is no longer recognizable by the end of the second cycle (shown in red). By the end of the third cycle, all the particles are deposited on the walls (shown as blue dots). Note that the extent of convective mixing of 0.5-μm particles is nearly equivalent or slightly higher than the extent of mixing induced by a phase difference between ductal flow oscillation and cyclic alveolar wall motion (Fig. 8*C*, $\delta = 20°$).

DISCUSSION

In previous models of alveolated ducts with rigid walls (5, 6, 25, 26), the acinar flow was typically treated as a flow consisting of two distinct flow regions. In the acinar ductal region, an axial flow streams by the alveolar openings without entering the alveoli, whereas, inside the alveoli, the flow rotates slowly without convectively communicating with the ductal region. Thus, according to these models, there is no convective transport of particles between acinar channels and the surrounding alveoli, and fine-sized aerosol particles that do not undergo Brownian motion can only enter the alveolus due to gravity. In the present study, we demonstrate that the inclusion of an additional factor, the rhythmical motion of the alveolar walls, fundamentally changes the acinar flow patterns and substantially alters the fate of particles moving inside the alveoli. Associated with tidal breathing, each alveolus expands and contracts about 12 times per minute; that is, the alveolar volume changes, necessarily inducing airflow between the duct and alveolus. This entering and exiting alveolar convective flow may carry aerosol particles into and outside the alveolus. The effects of alveolar convective airflow on small aerosol particles (e.g., 0.5 μm) are likely to be critical in the study of aerosol deposition in the pulmonary acinus, yet no existing model has dealt with this effect. The present work, therefore, represents the first systematic study focusing on this important issue.

It should be noted that our present analysis neglects the stochastic Brownian force exerted on a moving particle, whose influence relative to the gravity force, especially on small particles 0.5 μm in diameter, is still in dispute (e.g., Ref. 13) and might prove to be potentially important. Nevertheless, the exclusion of diffusion is necessary here, because the objective of this study is to perform, as a first step, a mechanistic analysis that would elucidate the fundamental physics of gravitational sedimentation coupled with particle convection in the complex, rhythmically expanding and contracting, chaotic alveolar flow, with the latter being so fundamentally different from the steady Poiseuille flow applied in many past investigations. Thorough investigation on the combined effects of Brownian motion and alveolar chaotic flow on small particles, as well as simultaneous effects of Brownian motion and gravitational sedimentation in complex alveolar flows, is left as future research topics.

Alveolar Flow

The basic premise of the present model is that alveolar flow can be considered as creeping (inertialess)

flow. We argue that this assumption is justifiable, at least as a first-order approximation, because the Reynolds number of airflow in the acinus is generally much smaller than unity. This also means that the "Reynolds number" is no longer relevant for inertialess flows; we must introduce a more appropriate parameter to characterize the alveolar flows. As our laboratory has been emphasizing in recent investigations (8, 11, 27), we proposed that λ, the ratio between Q_A and Q_D, multiplied by a constant and a local geometric factor $(R_D/R_0)^3$, should be the new important parameter[3] that characterizes alveolar flow. Because both Q_A and Q_D are proportional to a product of tidal volume (V_T) and ω, both V_T and ω are canceled out from the Q_A-to-Q_D ratio, and, therefore, λ is solely a function of acinar tree geometry. Our calculation (see APPENDIX B) shows that λ starts as a small number ($\sim 10^{-4}$) at the entrance of the acinus (16 $\sim$ 18th generations), exponentially increases as the tidal air moves deeper into the acinus, and becomes an order of unity at the most distal part of the acinus. In this paper, we use γ ($= 1/\lambda$), the reciprocal of λ, to express the relative importance between Q_D and Q_A.

In recent studies (8, 11, 27), we demonstrated that the inclusion of the cyclic motion of alveolar walls (represented by nonzero β in the present study) fundamentally changes acinar flow patterns. The detailed alveolar flow patterns, especially the presence (or absence) of recirculation flow inside the alveolus, depend largely on γ, which represents the relative strength of the axial thoroughfare ductal flow and the lateral alveolar entering and exiting flow. The larger the γ is (corresponding to the flow conditions in more proximal acinar generations), the more likely that alveolar recirculation flows occur and the larger the alveolar space the recirculating region occupies (see Fig. 5 in Ref. 8). On the other hand, when γ is small (e.g., <10; corresponding to the flow conditions in the postdistal region in the acinar tree), the alveolus hardly possesses a recirculating region, and the alveolar flow is largely radial (see Fig. 5 in Ref. 8). It should be noted that the presence (or absence) of alveolar recirculation is paramount in understanding the behavior of fine-sized particles in the alveolus, because introduction of a small phase lag can make the alveolar flow chaotic (8, 27).

In what follows, we focus our discussion on the effects of rhythmical motion of the alveolar walls on gravitational particle deposition inside the alveolus based on these two parameters, β and γ, separately.

Effects of β (Wall Motion)

The parameter β denotes the lung expansion strain.[4] In the analysis varying β from 0 (i.e., rigid walls) to 0.1 while keeping fixed the acinar ductal flow conditions, we compare the behavior of particles in an alveolus with moving walls ($\beta > 0$) to that of rigid ones ($\beta = 0$) (Table 1). The effect of wall motion is dramatic; the alveolar deposition efficiency can be more than doubled when the alveolar wall moves even to a very small degree (i.e., $\beta = 0.05$). This suggests that previous predictions based on the alveolar models with rigid walls (5, 6, 25, 26) might have substantially underestimated particle deposition inside the alveolus.

Effects of γ (Alveolus Location Along the Acinar Tree)

Varying γ and keeping β at a fixed physiologically relevant value ($\beta = 0.1$), we study the effects of alveolus location along the acinar tree on particle deposition. A strong dependence of alveolar entering efficiency, of particle trajectories, and of particle deposition sites within the alveolus on γ can be observed (Figs. 6 and 7). For alveoli near the acinar entrance (e.g., respiratory bronchioles) where ductal flow substantially dominates the alveolar lateral flow, the value of γ is large, and the strong ductal shear flow passing by the alveolar opening induces a large recirculation inside the alveolus. Consequently, the number of particles entering the alveolus mouth and moving inside the alveolus is largely influenced by this alveolar recirculation flow, with the particles moving quickly to the proximal side of the alveolar walls, where they are finally deposited (Fig. 6*B*, *top*, and Fig. 7). This basic airflow pattern and deposition mechanism persist in most of the alveoli along the acinar tree up until $\gamma > 100$. In this region of acinus, aerosols are quickly deposited, mostly during an inspiration period, consistent with experimental observation reported by Bennett and Smaldone (1). For small values of γ (<100) representing the alveolar flow conditions at the distal end of the acinus, however, the deposition process and deposition patterns are very different from the one described above. Deposition occurs continuously (Fig. 7), and the pattern of deposition inside the alveolus is largely uniform (Fig. 6*B*, *bottom*). This distinct difference of the $\gamma = 10$ from the $\gamma > 100$ cases is most probably due to the fact that, for $\gamma = 10$, there is no recirculating flow, and the flow is largely radial inside the alveolus. Thus the existence of alveolar recirculation and expansion is a key factor in determining deposition processes and deposition patterns.

Effects of Particle Size

Based on results shown in Figs. 3–6, aerosol particles considered in this study ($0.5 \sim 2.5$ μm) may be categorized into two size groups: submicron-sized particles ($0.5 < D_P \leq 1$ μm) and micron-sized particles ($1 < D_P < 2.5$ μm). Particles in the former size range are highly sensitive to the detailed instantaneous alveolar flow patterns, and, therefore, their trajectories are determined as a result of the competition between gravitational and alveolar aerodynamic forces. When γ is large (e.g., $\gamma > 1{,}000$), the gravitational deposition of submicron particles (e.g., $D_P = 0.5$ μm) occurs preferentially near the proximal side of the alveolar rim during early inspiration (Fig. 7). When γ is small (e.g., $\gamma < 10$), the submicron particles are deposited rather uniformly at the bottom of the alveolus and continu-

[3] In previous papers (8, 27), λ was expressed by the ratio Q_A/Q_D.

[4] The product of β and alveolar radius R_0 is the amplitude of alveolar wall expansion.

ously throughout both the inspiration and the expiration periods during a few breathing cycles (Fig. 7). These results suggest that the direction and magnitude of the gravitational force and the alveolar flow patterns must be known to make it possible to predict the characteristics of submicron particle deposition within the alveoli (i.e., timing and site as a function of alveolus location along the acinar tree). In contrast, larger particles (1 μm $< D_P <$ 2.5 μm) are generally not significantly influenced by the detailed alveolar flow patterns.

Convective Mixing and Enhanced Deposition Mechanisms

One of the most peculiar features of rhythmically expanding alveolar flow is that an alveolar flow with recirculation can be chaotic, enhancing mixing under the effect of small disturbances (8, 11, 24, 27). In previous studies, the effects of small nonzero Reynolds numbers (inertial effects) were addressed (11, 27), and the effects of a small-phase difference between ductal flow oscillation and cyclic alveolar wall motion were examined (8, 28). In the present study, we investigated gravitational effects on convective mixing by following particle trajectories (Fig. 8).

The terminal velocity of 0.5-μm particles with density of 1 g/cm^3 in quiescent air is ~10 μm/s. It means that, if gravity were the only mechanism driving deposition, it would take ~15 s (or 3–5 breaths) for the particle to move across a rigid-walled alveolus, 300 μm in diameter. This is a rather slow process. However, particles that are subjected to the combined effects of gravity and the complex flow existing inside the alveoli continuously cross streamlines, and their trajectories become increasingly convoluted. Thus substantial convective mixing occurs.

In a rhythmically expanding and contracting alveolus with characteristic recirculation flow, deposition is enhanced (Table 1). A possible qualitative explanation is as follows. Due to the expansion movement of the alveolar walls, the probability of aerosol particles crossing the alveolus mouth is enhanced [see Figs. 3, 4, and also Fig. 5 from Haber et al. (8) depicting streamlines that enter the alveolus]. After entering the alveolus, the circulating flow field carries the particles, conveying them closer to the alveolar walls. Near the walls, the tangential velocity is exceedingly small. Consequently, the particles would spend most of the time at the wall vicinity, increasing their probability of being deposited. Simultaneously, the particles are being pulled downward by gravity, a process that causes their final approach toward the alveolar wall. Note also that the deposition pattern can be highly nonuniform[5] (Fig. 8*B*), a very different pattern than would be conceived for the case of a rigid alveolus.

[5] Deposition occurs near the alveolar opening on both proximal and distal sides of alveolar walls, vertically higher than the original position of particle cloud [Fig. 8*B*; compare the vertical positions of blue dots (deposition sites) to the black square (original position)].

Physiological Implication

Comprehensive knowledge of aerosol deposition in the lung is needed so that the adverse effects of environmental particulate pollution can be understood and various therapeutic strategies of aerosolized drug delivery can be examined. Thus a large number of experimental investigations, both in animals and with human subjects, have been performed. Despite such considerable research efforts, much of the experimental data are limited to measurements of total particle deposition, and accurate assessments of regional deposition are still technically difficult. To complement this deficiency in an experimental approach, many mathematical models of aerosol deposition in the lungs have been developed, and our current knowledge of regional deposition is largely based on the predictions of these models (e.g., Ref. 15). The goal of the present study is to make model predictions of acinar deposition more realistic and accurate by incorporating an important factor, the rhythmical motion of alveolar walls.

At the level of alveolus. The alveolar surface is vulnerable to inhaled particles because the alveolar wall, in contrast to the well-protected, ciliated surface of conducting airways, is made of an ultrathin layer of epithelium to maximize the efficiency of gas exchange. Furthermore, this wall is not merely a simple layer of type I epithelial cells; it has its own structural complexity. For instance, smooth muscle is preferentially localized to the alveolar entrance rings (32), and sensory nerve endings are situated at specific locations within the alveolar wall (18). There is also a report that alveolar type II cells tend to be localized in the corners of the alveoli (35). The localization of particle deposition patterns within the alveolus, therefore, may have particular physiological implications. For instance, particles in the submicron-sized range would preferentially deposit near the entrance rings of the alveoli and especially in the proximal region of the acinus (i.e., high γ value). Because the alveolar entrance rings are rich with stress fibers and smooth muscle, and these components are important players for maintaining structure and dynamics of the lung parenchyma, a high dose of pollutants specifically concentrated on this region of the alveoli may result in adverse effects on respiratory function.

At the level of acinus. In the case of horizontally placed alveolus with its mouth upward, all of the particles entering the alveolus are eventually deposited. Therefore, the alveolar entering efficiency (η_i) shown in Fig. 6*A* can be utilized as the "local alveolar deposition probability" (although it does not mean that η_i represents a deposition probability of an alveolus in case a different gravity orientation, with respect to that of the alveolus axis, is employed) to compute deposition patterns along the acinar tree with rhythmically expanding and contracting alveolus compared with that of a rigid-walled alveolus.

The number of particles that are deposited in an alveolus at generation i is defined by a product of the local alveolar deposition probability η_i and the number

of particles available in the gas phase for that alveolus. Accounting for the fact that the number of particles in the gas phase decreases as the inhaled particles sample more and more alveoli along the acinar tree, the average number of particles c_i that are deposited in a single alveolus at the ith generation may be expressed as $c_i = C_{\text{total}} \cdot \{(1 - \eta_{16})^{n16} (1 - \eta_{17})^{n17} \ldots (1 - \eta_{i-1})^{n_{i-1}} [1 - (1 - \eta_i)^{n_i}]/2^{i-16} n_i\}$, where C_{total} is the total number of particles leaving a particular 15th generation duct and entering the acinar ducts, *generations 16–23*, and n_i denotes the number of alveoli attached to a single ith generation duct.

In Fig. 9, the ratio c_i/C_{total} as a function of the acinar generation number i is illustrated for 0.5-μm particles. A comparison is made between the classical rigid-walled and the rhythmically moving-wall alveolar models. According to the former model, the mean alveolar deposition is practically zero in the first three acinar generations (i = 16, 17, 18), peaks at the next two generations (i = 19, 20), and finally reduces to zero deep in the acinus (i = 22, 23). In the more realistic rhythmically expanding and contracting model, on the other hand, the local alveolar deposition starts high at the entrance to the acinus (i = 16), monotonically decreases in the first few generations (i = 17, 18, 19), and becomes practically zero in the last four acinar generations (i = 20, 21, 22, 23). These results suggest that *1*) predictions of deposition patterns along the acinar tree would unrealistically be compromised if one ignores the motion of alveolar walls, and *2*) the present model with alveolar wall motion predicts that deposition of 0.5-μm particles occurs in the first half of acinar pathway, with a preferentially higher deposition at the entrance of the acinus [see also Saldiva et al. (22), which agrees with our second conclusion].

It is interesting to point out that the present model predicts almost no deposition in the distal half of the acinus generation (i = 20–23), even though the distal local alveolar deposition probabilities are much higher than those in the proximal half of the acinus. This is due to the fact that, in the proximal region, the local alveolar deposition process, despite the associated, relatively low deposition probabilities ($0.1 < \eta_i < 0.2$, i = 16–19), consistently and significantly reduces the number of particles available for deposition in the distal region of the acinar tree. In the early 1980s, Weibel et al. (33) suggested that a similar phenomenon, called "screening," is likely to occur in the case of O_2 transport and recently demonstrated that "screening" is significantly influenced by acinar geometry and O_2 diffusion in the gas phase relative to its permeation through the alveolar surfaces (23). Based on the present study, we also conclude that "screening" may occur in the case of aerosol transport in the acinus, and it is largely influenced by alveolar wall characteristics (shape and motion) and the associated alveolar flow. Note that it is important to incorporate the concept of "screening and unscreening" when one interprets the local deposition distribution along the airway pathway from experimental measurements (e.g., Ref. 16, 17).

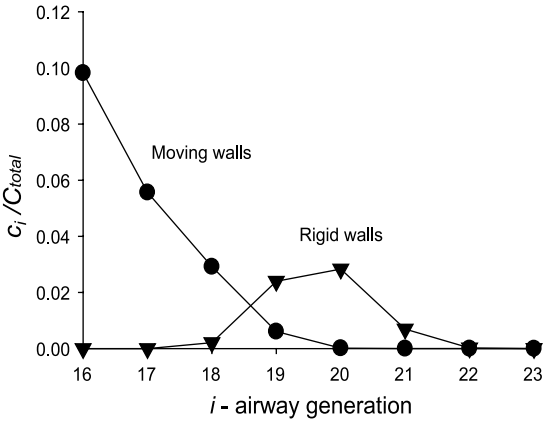

Fig. 9. The average no. of 0.5-μm particles, deposited in a single alveolus at the ith generation (c_i) normalized by the total no. of particles entering the acinus (C_{total}) is plotted against airway generation number. A comparison is made between the classic rigid-walled and the rhythmically moving-wall alveolar models.

At the level of the tracheobronchial tree. As we described, much of our current knowledge of local deposition in the lung is based on mathematical model predictions. To the best of our knowledge, however, none of the currently available mathematical models (except ours) incorporates the effects of expansion and contraction of the lungs, one of the most crucial determinants of particle deposition in the acinus, on local deposition. Therefore, even though the total deposition predicted by the "classical" models, calculated as the sum of local deposition values predicted for each airway compartment, corresponds well to the total deposition measured experimentally, the distribution of particle deposition along the tracheobronchial tree predicted by these models could be far from the one occurring in reality. The fact that the inclusion of alveolar wall motion in the present model results in much higher local acinar deposition than that by the classical model suggests that, in reality, more (less) particles are deposited in the proximal alveolar ducts (the conducting airways) than predicted previously.

Summary

Gravitational deposition processes and deposition sites in a rhythmically expanding and contracting alveoli differ from conventional predictions made by classical models, which treat the acinar duct as a straight pipe with rigid walls, and thus approximate gravitational deposition of particles immersed in unidirectional Poiseuille-like simple flows. We conclude that gravitational deposition in the pulmonary acinus is much more complex than assumed previously, and it is essential to incorporate the cyclic motion of alveolar walls to predict gravitational trajectories and deposition of fine particles.

APPENDIX A

The solution for $\mathbf{v}^{\text{H}}$ that was derived analytically (8) is axisymmetric and possesses only two independent velocity components v_ρ^{H} and v_z^{H} in the radial and axial directions, ρ and z, respectively, that depend on the two cylindrical coor-

dinates (ρ,z). Thus, in a Cartesian coordinate system, $\mathbf{v}^H$ possesses the following form[6]

$$\mathbf{v}^H = \begin{bmatrix} \nu_\rho^H(\rho, z) \cos(\phi) \\ \nu_\rho^H(\rho, z) \sin(\phi) \\ \nu_z^H(\rho, z) \end{bmatrix} \quad (A1)$$

where ϕ is the polar angle. The 3D solution for $\mathbf{v}^P$ was numerically obtained (21) utilizing the boundary element method. The numerical procedure was greatly simplified because the velocity's analytic dependence on the polar angle ϕ had been known a priori. Consequently, the velocity field depends on three independent unknown functions of the coordinates (ρ,z) to be determined numerically. The solution possesses the general following form in Cartesian coordinates[7]

$$\mathbf{v}^P = \begin{bmatrix} \nu_1^P(\rho, z) \cos(\phi) \sin(\phi) \\ \nu_1^P(\rho, z) \sin^2(\phi) + \nu_2^P(\rho, z) \\ \nu_3^P(\rho, z) \sin(\phi) \end{bmatrix} \quad (A2)$$

where the undisturbed shear flow far from the cavity points in the y direction.

APPENDIX B

Alveolar Flow

Assuming that an alveolus is represented by a hemisphere of radius R_0 (= 100 μm), the amplitude of a minute ventilatory flow, Q_A, entering and exiting each alveolus may be expresses as

$$Q_A = 2\pi R_0^3 \beta\omega \quad (B1)$$

where β is the tidal maximum strain of alveolar radius.

Ductal Flow

Using Weibel's counting system[8] of airway generation, a flow, Q_{D_n}, through an acinar duct of the generation n may be expressed as follows. We consider that the airflow entering the lung, Q_{ao}, is represented by a sum of flows, which enters the expanding and contracting acini (i.e., alveoli and associated acinar ducts). Because alveolar spaces are typically about three times larger than the volume of ductal region (9), Q_{ao} may be expressed as

$$Q_{ao} = \tfrac{4}{3} Q_A (N_{16} + N_{17} + \cdots + N_{23}) \quad (B2)$$

where N_n denotes the total number of alveoli at generation n. Based on Weibel's estimation (31), the total number of alveoli in the human lung is about three hundred million (i.e., $\sum_{n=16}^{23} N_n = 300 \times 10^6$), and the distribution of N_n is given as $N_{16} \approx 0.2 \times 10^6$ (a rough estimate), $N_{17} = 0.6 \times 10^6$, $N_{18} = 2.0 \times 10^6$, $N_{19} = 6.0 \times 10^6$, $N_{20} = 21.0 \times 10^6$, $N_{21} = 41.5 \times 10^6$, $N_{22} = 84.0 \times 10^6$, and $N_{23} = 143.0 \times 10^6$. Now, let us consider a flow through each acinar duct, Q_{D_n}, at generation n. It can be approximated as a difference between the total flow entering the lung, Q_{ao}, and the flows expanding the alveoli and the associated ducts proximal to generation n

$$Q_{D_n} = \frac{1}{2^n} \left[Q_{ao} - \frac{4}{3} Q_A (N_{16} + N_{17} + \cdots + N_n) \right] \quad (B3)$$

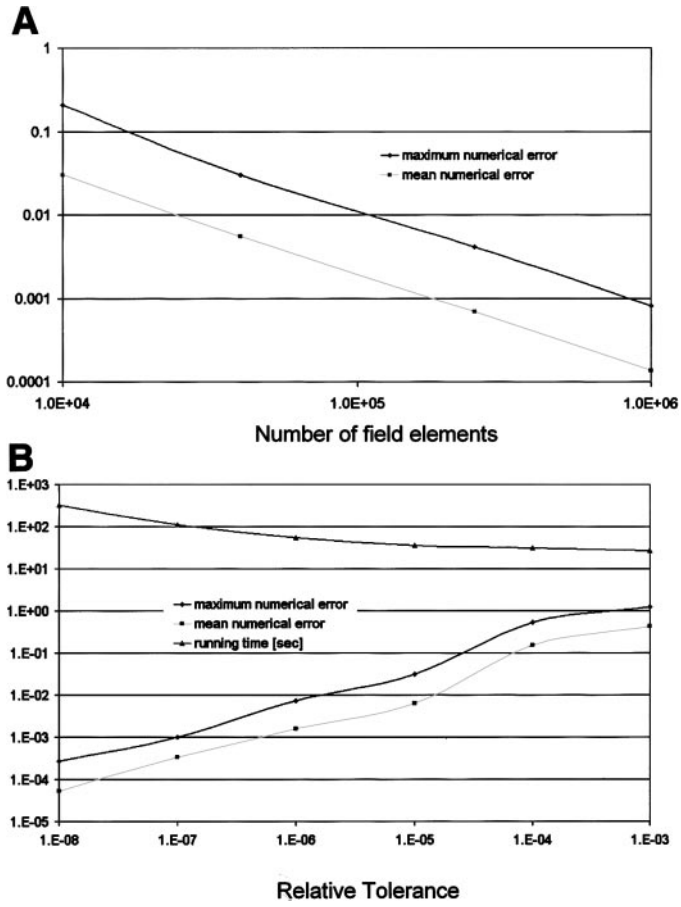

Fig. 10. *A*: maximum and mean numerical errors in particle trajectories vs. the no. of field elements for which the velocity field inside the alveolus was computed. *B*: maximum and mean errors in particle trajectory and solution running time vs. relative tolerance used in the ODE45 Matlab solver that determines the accuracy of the numerical integration.

Relative Ratio of Q_D to Q_A

As we discussed in the text, acinar flow may be better characterized by a dimensionless parameter, Q_{D_n}/Q_A, instead of the commonly used Reynolds number. Using *Eqs. B1* and *B3*, this ratio can be expressed

$$\frac{Q_{D_n}}{Q_A} = \frac{1}{2^n} \left[\frac{Q_{ao}}{Q_A} - \frac{4}{3} (N_{16} + N_{17} + \cdots + N_n) \right] \quad (B4)$$

Substituting *Eq. B2* into *Eq. B4*, and *Eq. 3* yields

$$\gamma = \frac{1}{3} 2^{-n+5} \left(\frac{R_0}{R_{D_n}} \right) \sum_{i=n+1}^{23} N_i \quad (B5)$$

Notice that γ depends only on the geometrical configuration of generation n down the acinar tree and is independent of lung kinematics such as V_T or ω.

[6] Haber et al. (8) express the solution in toroidal coordinates. However, a simple one-to-one correlation exists [see *Eq. 5* in Haber et al. (8)] between the toroidal and the cylindrical coordinates and the associated velocity components.

[7] Pozrikidis (21) provides explicit expressions for the velocity components in a cylindrical coordinate system. The transformation to a Cartesian coordinate system is straightforward.

[8] Based on the Weibel model (31), the acinus starts from *generation 16* at respiratory bronchiole and ends at *generation 23* (alveolar sac).

APPENDIX C

The vector field $\mathbf{v}^P$ was numerically obtained, and the values of v_1^P, v_2^P, and v_3^P (*Eq. A2*, see APPENDIX A) can be tabulated at given discrete nodal points in the ρ,z plane. The vector field $\mathbf{v}^H$ was analytically obtained and can, in principle, be calculated for every time step at any point in the ρ,z plane. However, it turns out to be more expedient to compute the velocity components v_ρ^H and v_z^H (see *Eq. A1* in APPENDIX A) at the same discrete nodal points and employ a two-dimensional linear interpolation method to obtain the velocity values at any place in the field. The same interpolation method is required to obtain $\mathbf{v}^P$ everywhere in the field with a similar error in velocity estimates. It is also advantageous to arrange the computed velocity data for v_1^P, v_2^P, v_3^P, v_ρ^H, and v_z^H in five matrices where the two indexes of a matrix element correspond to a location in the ρ,z plane and the element's value corresponds to the velocity component value at that location. An additional layer of fictitious nodal points external to the alveolus was added to enable interpolation near the alveolus wall. For the components of $\mathbf{v}^P$, zeroes were added (in accordance with the no-slip condition applied in this case), whereas, for the $\mathbf{v}^H$ components, the projection of a unity vector perpendicular to the wall was added (according to the expansion boundary condition that applies at the wall in this case). Matrix sizes of 100×100 were found to introduce large errors in particle trajectories, and only when we reached $1{,}000 \times 1{,}000$ sized matrices was the error reduced to an acceptable value (see Fig. 10*A*).

The differential equation (*Eq. 9*) was solved by using Matlab's ODE45 solver (2) with a relative tolerance equal to 10^{-8} and absolute tolerance of 10^{-16} that resulted in an acceptable error value (see Fig. 10*B*). Normally, errors can be computed by comparing results that are obtained by progressively refining mesh sizes, time steps, etc. In our case, however, we can also exploit the kinematic reversibility property of the Stokes equations. For example, if $\delta = 0$ and $H = 0$, trajectories must reverse during inhalation and exhalation, and the solution must be 2π periodic. Thus a test case has been defined with initial conditions $(\hat{x}_{p0}, \hat{y}_{p0}, \hat{z}_{p0}) = (0.2, -0.1, -0.8)$, $\gamma = 200$, and $D_p = 2$ μm, and the mean and maximum errors e_{av} and e_{max}, respectively, that appear in Fig. 10 were calculated by the respective L_1 and L_∞ norms as follows

$$e_{av} = \frac{1}{nm}\sum_{i=1}^{m}\sum_{j=1}^{n}|\Delta\hat{\mathbf{r}}_i(t_j)|, \quad e_{max} = \max|\Delta\hat{\mathbf{r}}_i(t_j)|$$

where $\Delta\hat{\mathbf{r}}_i(t_j) = \hat{\mathbf{r}}_i(t_j) - \hat{\mathbf{r}}_1(t_j)$, and $\hat{\mathbf{r}}_i(t_j)$ is the particle normalized location that it possessed during the i breathing cycle at time t_j (modulus 2π, the dimensionless breathing period). In other words, e_{av} illustrates the mean deviation between particle trajectory within breathing period i with that obtained after the first breathing period, during m periods sampled at n fixed times during the breathing periods. Figure 10 was obtained for $n = 50$ and $m = 20$. Notice that, generally, L_1 norms yield larger values than the more commonly used L_2 Euclid norms and, as such, define a more stringent accuracy test.

The solution process includes the following significant steps. The current particle position in Cartesian coordinates is transformed into cylindrical coordinates (ρ,ϕ,z). The (ρ,z) coordinates of the particle center are normalized with respect to alveolus time-dependent dimensionless radius $\hat{R}$. The functions v_1^P, v_2^P, v_3^P, v_ρ^H, and v_z^H at the normalized (ρ,z) plane are calculated utilizing the data matrices and a linear interpolation procedure. The velocity components are calculated by using *Eqs. A1*, *A2*, and *3*. Matlab's ODE45 procedure is applied on *Eq. 9* to obtain the new real dimensionless position of the particle center. The new position is utilized to examine whether the particle has or has not penetrated the alveolus or the duct walls. If penetration has occurred, a deposition site is registered, and the program terminates. Otherwise, the program continues running, returning to the first step described in the above. The program also terminates whenever the time exceeds a prescribed number of breathing periods or whenever the particle leaves the ductal volume adjacent to the alveolus and moves further up or down the alveolar tree.

The research is part of an MS thesis of D. Yitzhak submitted to the Senate of the Technion.

DISCLOSURES

This study was supported by the fund of promotion of research at the Technion, National Heart, Lung, and Blood Institute Grant HL-54885, and, in part, by Environmental Protection Agency Research Award R827353.

REFERENCES

1. **Bennett WD and Smaldone GC.** Inspiratory vs. expiratory aerosol deposition in excised dog lungs. *J Aerosol Sci* 18: 49–57, 1987.
2. **Biran A and Breiner M.** *Matlab 5 for Engineers.* Boston, MA: Addison-Wesley, 1999.
3. **Brain JD and Valberg PA.** Deposition of aerosol in the respiratory tract. *Am Rev Respir Dis* 120: 1325–1373, 1979.
4. **Butler JP and Tsuda A.** Effect of convective stretching and folding on aerosol mixing deep in the lung, assessed by approximate entropy. *J Appl Physiol* 83: 800–809, 1997.
5. **Darquenne C.** A realistic two-dimensional model of aerosol transport and deposition in the alveolar zone of the human lung. *J Aerosol Sci* 32: 1161–1174, 2001.
6. **Darquenne C and Paiva M.** Two- and three-dimensional simulations of aerosol transport and deposition in alveolar zone of human lung. *J Appl Physiol* 80: 2889–2898, 1996.
7. **Fuch NA.** *The Mechanics of Aerosols.* Oxford, NY: Pergamon, 1964.
8. **Haber S, Butler JP, Brenner H, Emanuel I, and Tsuda A.** Shear flow over a self-similar expanding pulmonary alveolus during rhythmical breathing. *J Fluid Mech* 405: 243–268, 2000.
9. **Haefeli-Bleuer B and Weibel ER.** Morphometry of human pulmonary acinus. *Anat Rec* 220: 401–414, 1988.
10. **Happel J and Brenner H.** *Low Reynolds Number Hydrodynamics: With Special Applications to Particulate Media.* Boston, MA: Kluwer, 1983.
11. **Henry FS, Butler JP, and Tsuda A.** Kinematically irreversible acinar flow: a departure from classical dispersive aerosol transport theories. *J Appl Physiol* 92: 835–845, 2002.
12. **Heyder J.** Gravitational deposition of aerosol particles within a system of randomly oriented tubes. *J Aerosol Sci* 6: 133–137, 1975.
13. **Heyder J, Gebhart J, and Scheuch G.** Interaction of diffusional gravitational particle transport in aerosols. *Aerosol Sci Technol* 4: 315–326, 1985.
14. **Hung KS, Hertweck MS, Hardy JD, and Loosli CG.** Innervation of pulmonary alveoli of mouse lung: an electron microscopic study. *Am J Anat* 135: 477–495, 1972.
15. **ICRP.** *Human Respiratory Tract Model for Radiological Protection: A Report of a Task Group of the International Commission on Radiological Protection. ICRP Publication 66, Annals of the ICRP.* New York: Pergamon, 1994.
16. **Kim CS, Hu SC, Dewitt P, and Gerrity TR.** Assessment of regional deposition of inhaled particles in human lungs by serial bolus delivery method. *J Appl Physiol* 81: 2203–2213, 1996.
17. **Kim CS and Jaques PA.** Respiratory dose of inhaled ultrafine particles in healthy adults. *Philos Trans R Soc Lond A Math Phys Sci* A358: 2693–2705, 2000.

18. **Meyrick B and Reid L.** Nerves in rat intra-acinar alveoli: an electron microscopic study. *Respir Physiol* 11: 357–377, 1971.
19. **Miki H, Butler JP, Rogers RA, and Lehr J.** Geometric hysteresis in pulmonary surface to volume ratio during tidal breathing. *J Appl Physiol* 75: 1630–1636, 1993.
20. **Pich J.** Theory of gravitational deposition of particles from laminar flows in channels. *J Aerosol Sci* 3: 351–361, 1972.
21. **Pozrikidis C.** Shear flow over a plane wall with an axisymmetric cavity or a circular orifice of finite thickness. *Phys Fluids* 6: 68–79, 1994.
22. **Saldiva PHN, Clarke RW, Coull BA, Stearns RC, Lawrence J, Krishna Murthy GG, Diaz E, Koutrakis P, Suh H, Tsuda A, and Godleski JJ.** Lung inflammation induced by concentrated air particles is related to particle composition. *Am J Respir Crit Care Med* 165: 1610–1617, 2002.
23. **Sapoval B, Filoche M, and Weibel ER.** Smaller is better—but not too small: a physical scale for the design of the mammalian pulmonary acinus. *Proc Natl Acad Sci USA* 99: 10411–10416, 2002.
24. **Tippe A and Tsuda A.** Recirculating flow in an expanding alveolar model: experimental evidence of flow-induced mixing of aerosols in the pulmonary acinus. *J Aerosol Sci* 31: 979–986, 2000.
25. **Tsuda A, Butler JP, and Fredberg JJ.** Effects of alveolated duct structure on aerosol kinetics. I. Diffusional deposition in the absence of gravity. *J Appl Physiol* 76: 2497–2509, 1994.
26. **Tsuda A, Butler JP, and Fredberg JJ.** Effects of alveolated duct structure on aerosol kinetics. II. Gravitational sedimentation and inertial impaction. *J Appl Physiol* 76: 2410–2516, 1994.
27. **Tsuda A, Henry FS, and Butler JP.** Chaotic mixing of alveolated duct flow in rhythmically expanding pulmonary acinus. *J Appl Physiol* 79: 1055–1063, 1995.
28. **Tsuda A, Otani Y, and Butler JP.** Acinar flow irreversibility caused by perturbations in reversible alveolar wall motion. *J Appl Physiol* 86: 977–984, 1999.
29. **Tsuda A, Rogers RA, Hydon PE, and Butler JP.** Chaotic mixing deep in the lung. *Proc Natl Acad Sci USA* 99: 10173–10178, 2002.
30. **Wang CS.** Gravitational deposition of particles from laminar flows in inclined channels. *J Aerosol Sci* 6: 191–204, 1975.
31. **Weibel ER.** *Morphology of the Lung.* New York: Academic, 1963.
32. **Weibel ER.** Functional morphology of lung parenchyma. In: *Handbook of Physiology. The Respiratory System. Mechanics of Breathing.* Bethesda, MD: Am. Physiol. Soc., 1986, sect. 3, vol. III, pt. 1, chapt. 8, p. 89–111.
33. **Weibel ER, Taylor CR, Gehr P, Hopperler H, Mathieu O, and Maloiy GMO.** Design of the mammalian respiratory system. IX. Functional and structural limits for oxygen flow. *Respir Physiol* 44: 151–164, 1981.
34. **Wilson R and Spengler JD.** *Particles in Our Air*. Boston, MA: Harvard Univ. Press, 1996.
35. **Young SL, Fram EK, and Craig BL.** Three-dimensional reconstruction and quantitative analysis of rat lung type II cells: a computer-based study. *Am J Anat* 174: 1–14, 1985.
36. **Zeltner TB, Sweeney TD, Skornik WA, Feldman HA, and Brain JD.** Retention and clearance of 0.9-mm particles inhaled by hamsters during rest or exercise. *J Appl Physiol* 70: 1137–1145, 1991.